

Sensor free, self regulating thermal switching via anomalous Ettingshausen effect and spin reorientation in DyCo₅

Shibo Wang,¹ Hiroki Tsuchiura,^{1, a)} and Nobuaki Terakado^{1,2}

¹⁾*Department of Applied Physics, Tohoku University, Aoba, Sendai 980-8579, Japan*

²⁾*Department of Material Chemistry, Kyoto University, Katsura, Nishikyo-ku, Kyoto 615-8520, Japan*

We propose a sensor free, self regulating thermal switch that combines the anomalous Ettingshausen effect (AEE) with a temperature driven spin reorientation transition (SRT) in the rare earth cobalt compound DyCo₅. Using density functional theory and the Kubo linear-response formalism, we compute the anomalous Hall conductivity $\sigma_{xy}(\varepsilon)$ and the finite temperature anomalous Nernst conductivity $\alpha_{xy}(T)$ for two magnetization directions, $\mathbf{M} \parallel c$ and $\mathbf{M} \perp c$. While the intrinsic σ_{xy} at the Fermi level remains sizable for both orientations, α_{xy} exhibits about two orders of magnitude contrast in the SRT temperature window. This contrast is consistent with the low temperature Mott relation through the energy slope $\partial_\varepsilon \sigma_{xy}(\varepsilon)|_{E_F}$ and is traced to strongly peaked Berry curvature hot spots generated by spin orbit coupling induced avoided crossings of Co 3d bands. Combining α_{xy} with longitudinal transport coefficients, we estimate device level metrics, namely the anomalous Nernst thermopower S_{ANE} and the Ettingshausen coefficient $\Pi_{AEE} = TS_{ANE}$, and demonstrate robust orientation controlled switching under a fixed in plane bias current. These results establish a materials based route to compact thermal control without external sensors or feedback electronics and provide a concrete example that the proposed principle can be realized in an existing ferromagnet.

Modern microelectronic and energy systems increasingly require thermal control that is compact, localized, and as rapid as practicable^{1,2}. These requirements point to electrically driven mechanisms that are readily integrable on chip. Among such mechanisms, transverse thermoelectric effects (TTEs)³, notably the anomalous Nernst effect (ANE)⁴ and anomalous Ettingshausen effect (AEE)⁵, are attractive because they can operate without externally applied magnetic fields (e.g., field coils), once a ferromagnetic state provides spontaneous magnetization, and are governed by the Berry curvature of ferromagnets⁶. Their magnitudes, and even signs, are highly sensitive to the magnetization orientation, thereby providing a direct, materials-intrinsic means for functional control. However, most switching concepts still rely on external sensors or feedback electronics to determine when to reverse the heat flow. Unlike approaches where the magnetization is actively re-oriented by an externally applied magnetic field, strain, or current-induced torques, the present concept uses an intrinsic temperature-driven spin reorientation transition (SRT) as the internal “trigger.” This makes the switching threshold materials-defined and enables sensor-free negative feedback: once the device temperature enters the SRT interval, the equilibrium \mathbf{M} rotates and the AEE heat flux is redirected without external sensing or control circuitry.

In this context, a large AEE has recently been reported in SmCo₅-type permanent magnets⁷. These results motivate exploring related RCo₅ compounds with additional internal control parameters, including DyCo₅

which exhibits a temperature-driven spin-reorientation transition^{8,9}.

Herein, we propose a sensor-free, self-regulating thermal switch that leverages the AEE in DyCo₅, a member of the RCo₅ family that is known to exhibit an SRT^{8,10,11}. In this material, the magnetic easy axis rotates with temperature due to competing crystal-field and exchange anisotropies^{12,13}; it lies in-plane for $T < T_{SR1} \approx 325$ K and switches to the c axis at higher temperatures (with $T > T_{SR2} \approx 367$ K)^{8,10}. As T passes through the SRT interval, $T_{SR1} \lesssim T \lesssim T_{SR2}$, the magnetization \mathbf{M} reorients from in-plane toward the c axis. Under a fixed in-plane bias current \mathbf{J}_c , this reorientation toggles the transverse anomalous Nernst conductivity α_{xy} and thus the AEE-induced heat flux $\mathbf{J}_q \propto \alpha_{xy}$, enabling temperature-thresholded directional switching or modulation of heat flow without any external sensing. A schematic of the device concept is shown in Fig.1.

To establish the mechanism and quantify performance, we combined density-functional calculations and the Kubo linear-response formalism to evaluate the energy-resolved anomalous Hall conductivity $\sigma_{xy}(\varepsilon)$ and the finite-temperature $\alpha_{xy}(T)$. We found that although the intrinsic σ_{xy} at E_F remains sizable for both magnetization orientations of \mathbf{M} , α_{xy} changes by several orders of magnitude across the SRT. This contrast is consistent with the low- T Mott relation through the energy slope $(\partial_\varepsilon \sigma_{xy})|_{E_F}$ ^{14,15}, reflecting orientation-driven redistribution of Berry curvature near E_F . Device-relevant figures of merit, namely the ANE thermopower S_{ANE} and the Ettingshausen coefficient $\Pi_{AEE} = TS_{ANE}$ ¹⁶, exhibit robust, orientation-controlled switching at a fixed temperature (e.g., 300 K), highlighting a materials-integrated route to compact, current-driven, sensor-free thermal control.

^{a)} Author to whom correspondence should be addressed: tsuchi@tohoku.ac.jp

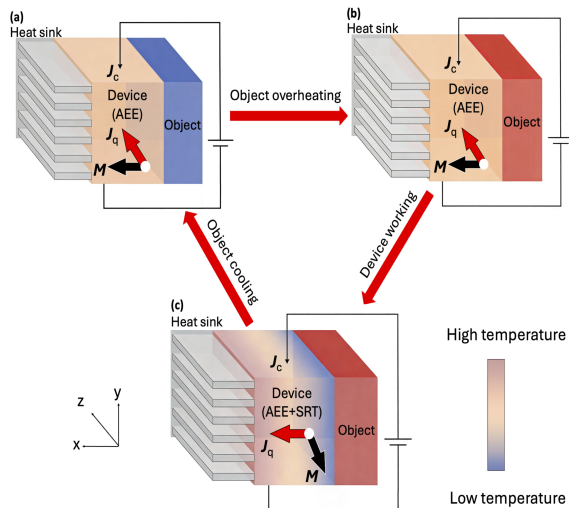


FIG. 1: Schematic of a self regulating thermal control device based on the anomalous Ettingshausen effect (AEE) and a spin reorientation transition (SRT). Here, T denotes temperature, \mathbf{M} magnetization, \mathbf{J}_c charge current density, and \mathbf{J}_q heat current density. Under a constant in-plane \mathbf{J}_c , AEE generates a transverse \mathbf{J}_q whose direction is set by \mathbf{M} . If the object is heated by δT , the device warms accordingly and, upon entering the SRT interval, \mathbf{M} reorients ($\perp z \leftrightarrow \parallel z$), which redirects or reverses \mathbf{J}_q . This provides a negative-feedback response: heat is drawn from the object in the overheated state and the system relaxes back toward the baseline temperature without external sensing.

Theoretical methods. We performed density functional theory (DFT) calculations using the full-potential linearized-augmented plane-wave (FP-LAPW) method¹⁷. Spin-orbit coupling (SOC) is treated self-consistently within the second-variational FP-LAPW scheme. Unless otherwise noted, the rare-earth $4f$ states are treated in the generalized gradient approximation (GGA)¹⁸ with a Hubbard correction U ¹⁹, and a moderate on-site interaction on Co $3d$ is used only to test the robustness of trends. We utilized the Wannier90 program²⁰ to construct maximally localized Wannier functions (MLWFs), which were then employed for Wannier interpolation to evaluate the Berry curvature. MLWFs²¹ are constructed primarily from Co $3d$ and s states (with rare-earth f) to reproduce the DFT bands. Longitudinal thermoelectric properties were computed within semi-classical Boltzmann transport theory as implemented in BoltzTraP2²². In the present work, Wannier90 (MLWF interpolation) is used to construct an MLWF-based tight-binding model and analyze the Berry curvature, while σ_{xy} and α_{xy} are obtained from Brillouin-zone (BZ) integrals of the Kubo expressions in WIEN2k. BoltzTraP2 is used only for σ_{yy}/τ and S_{yy} within the constant relaxation time approximation required for Eq. (6). Two

magnetization configurations were considered throughout: $\mathbf{M} \parallel c$ and $\mathbf{M} \perp c$ (in-plane). BZ quantities were evaluated on a dense $68 \times 68 \times 73$ k -mesh; all energy-resolved and finite- T integrals were examined for k -mesh convergence.

The intrinsic anomalous Hall conductivity (AHC) and anomalous Nernst conductivity (ANC), denoted by α_{xy} , are computed from the k -space Berry curvature within the Kubo linear-response formalism:

$$\sigma_{xy} = -\frac{e^2}{\hbar} \sum_n \int_{\text{BZ}} \frac{d^3\mathbf{k}}{(2\pi)^3} f_{n\mathbf{k}} \Omega_{n,z}(\mathbf{k}), \quad (1)$$

$$\alpha_{xy} = \frac{e}{\hbar} \sum_n \int_{\text{BZ}} \frac{d^3\mathbf{k}}{(2\pi)^3} \Omega_{n,z}(\mathbf{k}) s_{n\mathbf{k}}, \quad (2)$$

where $f_{n\mathbf{k}} = f(\varepsilon_{n\mathbf{k}})$ is the Fermi-Dirac factor and $s_{n\mathbf{k}} = -k_B [f_{n\mathbf{k}} \ln f_{n\mathbf{k}} + (1 - f_{n\mathbf{k}}) \ln (1 - f_{n\mathbf{k}})]$ is the entropy density per state^{23,24}. The Berry curvature follows from

$$\Omega_n(\mathbf{k}) = \nabla_{\mathbf{k}} \times \mathbf{A}_n(\mathbf{k}), \quad \mathbf{A}_n(\mathbf{k}) = i \langle u_{n\mathbf{k}} | \nabla_{\mathbf{k}} | u_{n\mathbf{k}} \rangle, \quad (3)$$

where $|u_{n\mathbf{k}}\rangle$ are cell-periodic Bloch states. Equations (1)–(3) fix our sign and derivative conventions.

For interpretability we also employ the energy resolved AHC representation,

$$\alpha_{xy} = -\frac{1}{eT} \int d\varepsilon \left(-\frac{\partial f}{\partial \varepsilon} \right) (\varepsilon - \mu) \sigma_{xy}(\varepsilon), \quad (4)$$

which reduces in the low temperature limit ($k_B T \ll E_F$) using the Sommerfeld expansion to the Mott relation:

$$\alpha_{xy} \simeq -\frac{\pi^2 k_B^2 T}{3e} \left. \frac{\partial \sigma_{xy}(\varepsilon)}{\partial \varepsilon} \right|_{\varepsilon=E_F}. \quad (5)$$

Equation (5) is used as an *intuition aid*; all quantitative results are obtained from Eqs. (2) and (4) at finite T . We next connect α_{xy} to device relevant thermoelectric metrics.

Device relevant metrics, the transverse thermopower due to ANE and the Ettingshausen coefficient, are related by the Kelvin relation $\Pi_{\text{AEE}} = T S_{\text{ANE}}$. Under open circuit conditions in the transverse direction and for a small Hall angle, we use²⁵

$$S_{\text{ANE}} \approx \frac{\alpha_{xy}}{\sigma_{yy}} - S_{yy} \frac{\sigma_{xy}}{\sigma_{yy}}, \quad (6)$$

where σ_{yy} and S_{yy} are the longitudinal conductivity and Seebeck coefficient along the current direction. While AHC and α_{xy} are determined by the Berry curvature in our formulation, the longitudinal conductivity depends on scattering. We therefore compute σ_{yy}/τ and S_{yy} using BoltzTraP2 within the constant relaxation time approximation. In this approximation S_{yy} is insensitive to the absolute value of τ , whereas σ_{yy} requires τ . We estimate

TABLE I: Relaxation times used in the constant relaxation time approximation. The conductivity σ values are taken from Refs.^{7,26}, and the present table was compiled by the authors (it is not reproduced or adapted from any published table).

System	τ (fs)	Basis
SmCo ₅ (bulk)	11.3	σ taken from Ref. ⁷ and our σ/τ
DyCo ₅ (thick film)	12.7	σ taken from Ref. ²⁶ and our σ/τ

τ by comparing calculated σ_{yy}/τ with reported experimental conductivities of $R\text{Co}_5$ compounds, and adopt $\tau = 11.3$ fs and $\tau = 12.7$ fs as representative values. Representative values are summarized in Table I. We report S_{ANE} and Π_{AEE} for both values to indicate the uncertainty associated with τ . We note that τ can be temperature dependent and may be further reduced near the SRT due to enhanced magnetic fluctuations and spin-disorder scattering. Such effects primarily rescale the longitudinal conductivity entering Eq. (6), whereas the key on/off contrast discussed here originates from the intrinsic α_{xy} computed from the Berry-curvature formulation.

We report AHC in S/m (1 S/cm = 100 S/m), the anomalous Nernst conductivity α_{xy} in $\text{A m}^{-1} \text{K}^{-1}$, S_{ANE} in $\mu\text{V}/\text{K}$, and Π_{AEE} in μV . Energies are referenced to E_{F} (shown as $E_{\text{F}} = 0$ in energy resolved plots). Colors and line styles are maintained identical across panels to distinguish $\mathbf{M} \parallel c$ and $\mathbf{M} \perp c$.

Energy-resolved anomalous Hall and Nernst responses. Figure 2 summarizes key transport coefficients of DyCo₅ as functions of the chemical potential μ within a rigid band approximation, where $\mu = 0$ corresponds to the Fermi level E_{F} . Figure 2(a) shows the anomalous Hall conductivity $\sigma_{xy}(\mu)$ for the two magnetization directions. Both configurations sustain a sizable intrinsic AHC at $\mu = 0$, whereas the detailed energy dependence near E_{F} differs between $\mathbf{M} \parallel (001)$ and $\mathbf{M} \parallel (100)$. For reference, the AHC values at $\mu = 0$ for the two magnetization directions are summarized in Table II. Figure 2(b) shows the anomalous Nernst conductivity $\alpha_{xy}(\mu)$ obtained from the same DFT bands and k mesh. A central observation is that the orientation dependence is modest in σ_{xy} but becomes dramatic in α_{xy} , reaching about two orders of magnitude contrast near $\mu = 0$. This behavior is consistent with the Mott relation in the low temperature limit, in which α_{xy} is governed by the energy slope $\partial_{\varepsilon}\sigma_{xy}(\varepsilon)|_{E_{\text{F}}}$ and hence is strongly affected by how Berry curvature is distributed in energy within the thermal window.

In terms of the energy-resolved AHC $\sigma_{xy}(\varepsilon)$, the slope $\partial_{\varepsilon}\sigma_{xy}$ is controlled by the Berry-curvature density at energy ε (i.e., by how much integrated Berry curvature is accumulated when the chemical potential is moved). Because SOC generates narrow avoided crossings carrying large Berry curvature, even a small magnetization-induced shift of these features by a few meV relative to E_{F} can strongly change $\partial_{\varepsilon}\sigma_{xy}|_{E_{\text{F}}}$ while leaving $\sigma_{xy}(E_{\text{F}})$ comparatively less affected. This explains why the orien-

TABLE II: AHC value at E_{F} in the (100) and (001) directions.

	$\mathbf{M} \parallel (100)$	$\mathbf{M} \parallel (001)$
AHC [$\times 10^4 \text{S/m}$]	6.18	11.80

TABLE III: α_{xy} value at E_{F} in the (100) and (001) directions for $T = 300$ K and $T = 400$ K.

α_{xy} [$\text{K}^{-1} \text{A m}^{-1}$]	$\mathbf{M} \parallel (100)$	$\mathbf{M} \parallel (001)$
$T = 300\text{K}$	0.0497	9.20
$T = 400\text{K}$	0.131	10.4

tation sensitivity is amplified in α_{xy} compared with σ_{xy} . **Berry curvature origin of the contrast.** To identify the microscopic origin of the orientation contrast, Fig. 3 presents the band dispersion and the Berry curvature along the high symmetry path $\Gamma \rightarrow M \rightarrow K \rightarrow \Gamma \rightarrow A$ for $\mathbf{M} \parallel c$ and $\mathbf{M} \perp c$. While Fig. 3 shows a one-dimensional high-symmetry cut for visualization, all reported σ_{xy} and α_{xy} values are obtained from full three-dimensional BZ integrals on the dense k mesh. The Berry curvature shown in the lower panels is the sum over the occupied states, $\Omega_z(\mathbf{k}) = \sum_n f(\varepsilon_{n\mathbf{k}}) \Omega_{n,z}(\mathbf{k})$, which corresponds to the integrand of the intrinsic anomalous Hall conductivity up to a constant prefactor. In both magnetization configurations, $\Omega_z(\mathbf{k})$ is nearly zero over most of the path but exhibits two strongly peaked hot spots on the $\Gamma \rightarrow A$ segment with opposite signs. These peaks originate from spin orbit coupling gaps at band (avoided) crossings among Co 3d derived states, for example involving d_{z^2} with d_{xz} and $d_{x^2-y^2}/d_{xy}$ characters, which generate large $\Omega_{n,z}$. Upon reorienting \mathbf{M} , the hot spot intensity is redistributed and their positions shift slightly along $\Gamma \rightarrow A$, leading to a modest change in the separation between the two peaks. This redistribution reshapes $\sigma_{xy}(\varepsilon)$ near E_{F} and hence modifies the energy slope that controls α_{xy} , providing a consistent explanation of the trends in Fig. 2(a,b). A detailed microscopic analysis of the origin of the positional shift is beyond the scope of the present work and is left for future study.

Robustness and consistency checks. All qualitative conclusions persist upon (i) modest variations of the onsite interaction on Co-3d (used only as a robustness check), (ii) enlarging the Wannierization window, and (iii) further refining the k mesh beyond $68 \times 68 \times 73$. Low T behavior follows the Mott relation, and finite T deviations track nonlinearity in $\sigma_{xy}(\varepsilon)$ within the thermal window. Device metrics S_{ANE} and Π_{AEE} are evaluated using longitudinal coefficients from the same band model and a single relaxation time τ appropriate to a given crystal quality; comparisons are made at a common temperature (300 K).

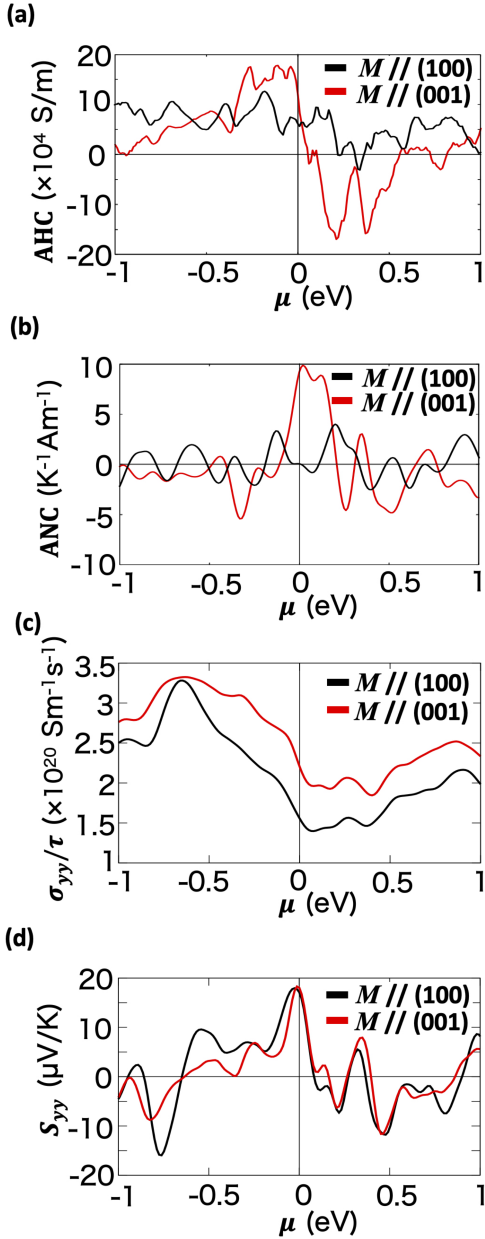


FIG. 2: Transport coefficients of DyCo₅ as functions of the chemical potential μ for two magnetization directions, $\mathbf{M} \parallel (100)$ and $\mathbf{M} \parallel (001)$. The chemical potential is varied within a rigid band approximation to indicate the carrier doping trend, and $\mu = 0$ corresponds to the Fermi level (E_F). (a) Anomalous Hall conductivity (AHC) $\sigma_{xy}(\mu)$ in units of 10^4 S/m. (b) Anomalous Nernst conductivity $\alpha_{xy}(\mu)$ in units of $\text{A m}^{-1} \text{K}^{-1}$. (c) Longitudinal conductivity shown as $\sigma_{yy}(\mu)/\tau$ in units of $10^{20} \text{ S m}^{-1} \text{ s}^{-1}$, where τ is the relaxation time. (d) Longitudinal Seebeck coefficient $S_{yy}(\mu)$ in units of $\mu\text{V/K}$. Panels (c) and (d) provide the longitudinal inputs required to evaluate the transverse thermopower due to ANE, S_{ANE} , via Eq. (6). A common color scheme is used across panels to distinguish $\mathbf{M} \parallel (100)$ and $\mathbf{M} \parallel (001)$.

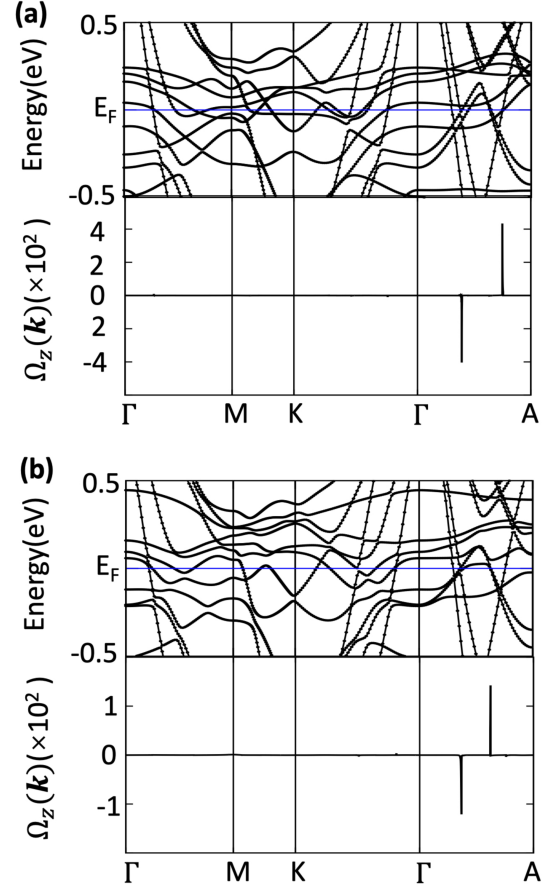


FIG. 3: Band dispersion and Berry curvature of DyCo₅ along the high symmetry path $\Gamma \rightarrow M \rightarrow K \rightarrow \Gamma \rightarrow A$ within the energy window $-0.5 \text{ eV} < E < 0.5 \text{ eV}$. The upper panels show the band dispersion, while the lower panels plot the Berry curvature summed over occupied states, $\Omega_z(\mathbf{k}) = \sum_n f(\varepsilon_{n\mathbf{k}}) \Omega_{n,z}(\mathbf{k})$, which corresponds to the integrand of the intrinsic anomalous Hall conductivity up to a constant prefactor. (a) $\mathbf{M} \parallel c$ and (b) $\mathbf{M} \perp c$. In both cases $\Omega_z(\mathbf{k})$ is nearly zero over most of the path but exhibits two sharply peaked hot spots along $\Gamma \rightarrow A$, with opposite signs near Γ and near A . Upon reorienting \mathbf{M} , the hot spot positions shift slightly along $\Gamma \rightarrow A$, resulting in a modest change in the separation between the two peaks. These hot spots coincide with band (avoided) crossings of Co 3d states in the dispersion, indicating that the orientation dependence of the thermoelectric Hall response originates from Berry curvature hot spots generated by spin orbit coupling near band degeneracies. The hot-spot energies shift upon reorienting \mathbf{M} because the SOC term $\lambda \mathbf{L} \cdot \mathbf{S}$ couples orbital characters differently for different spin-quantization axes: rotating \mathbf{M} changes the SOC matrix elements and the pattern of hybridization gaps at near-degenerate Co-3d crossings, thereby moving the avoided-crossing energies (and associated Berry-curvature peaks) relative to E_F . For clarity, this plot is a 1D cut used for visualization; the quantitative σ_{xy} and α_{xy} are evaluated from full 3D BZ integrals.

Room temperature snapshot and implications. At $T = 300$ K, DyCo_5 exhibits a large intrinsic AHC for both magnetization orientations, whereas α_{xy} shows a pronounced orientation contrast under identical conditions. To provide an order-of-magnitude device estimate, we model a DyCo_5 slab of thickness t carrying an in-plane current density J_c , for which the AEE generates a transverse heat flux $J_q \approx \Pi_{\text{AEE}} J_c$ (W m^{-2}). Using the small-Hall-angle approximation $S_{\text{ANE}} \simeq \rho_{yy} \alpha_{xy}$ (with $\rho_{yy} = 1/\sigma_{yy}$) and the Kelvin relation $\Pi_{\text{AEE}} = T S_{\text{ANE}}$, this can also be written as $J_q \approx T \alpha_{xy} \rho_{yy} J_c$. In steady state, this produces a transverse temperature drop $\Delta T_{\text{AEE}} \sim J_q t / \kappa$, where κ is the effective thermal conductivity across the slab. Using the room-temperature values at $\mu = 0$ (Table III) together with a representative metallic conductivity $\sigma_{yy} \sim 10^6\text{--}10^7$ S/m, we obtain $S_{\text{ANE}} \sim \alpha_{xy} / \sigma_{yy} \approx 1\text{--}10$ $\mu\text{V/K}$ in the high- α_{xy} orientation and about two orders of magnitude smaller in the low- α_{xy} orientation, implying $\Pi_{\text{AEE}} \sim 0.3\text{--}3$ mV at 300 K. For current densities $J_c \sim 10^9\text{--}10^{10}$ A/m² and $t \sim 1\text{--}10$ μm (with $\kappa \sim 10\text{--}30$ W/mK), this corresponds to $\Delta T_{\text{AEE}} \sim 0.1\text{--}10$ K, providing experimentally visible contrast and negative feedback once the device temperature enters the SRT window ($T_{\text{SR1}} \approx 325$ K to $T_{\text{SR2}} \approx 367$ K). The resulting transport scales (AHC of order $10^2\text{--}10^3$ S/cm and ANE thermopower of order $\mu\text{V/K}$) are consistent with reported values for metallic ferromagnets and Co-based magnets, supporting the plausibility of the magnitudes shown in Fig. 2^{3,6}.

Experimentally, the effect can be probed in a DyCo_5 thin film patterned into a Hall-bar geometry: an in-plane current J_c is applied while the transverse temperature profile (or heat-flow direction) is detected using microthermometry (e.g., resistance thermometers or thermocouples) or scanning thermal/IR thermography on the film surface. Such a film-based implementation directly targets an application scenario of on-chip thermal regulation, where the SRT provides a built-in temperature threshold for autonomous control.

The resulting difference in S_{ANE} and Π_{AEE} enables a *sensor free but current driven* thermal switch whose state is set by the materials' internal SRT threshold. Beyond DyCo_5 , the mechanism—reorientation driven relocation of Berry curvature hot spots near E_F —suggests a practical “tuning knob” for $R\text{Co}_5$ and related ferromagnets: Selecting compositions and strain states that sharpen $\partial_\varepsilon \sigma_{xy}$ near E_F will enhance α_{xy} and improve switching contrast, as long as longitudinal losses remain modest.

To summarize, we proposed and quantified a *sensor-free, self-regulating* thermal switch that combines the AEE with a temperature-driven SRT in $R\text{Co}_5$. Using DFT-Kubo calculations, we established a one-pathway mechanism from the energy-resolved anomalous Hall conductivity $\sigma_{xy}(\varepsilon)$ to the finite-temperature anomalous Nernst conductivity $\alpha_{xy}(T)$. Although the intrinsic AHC at E_F remains sizable for both $\mathbf{M} \parallel c$ and $\mathbf{M} \perp c$, α_{xy} exhibits a pronounced orientation contrast

across T_{SRT} . The effect is traced to the *energy slope* $\partial_\varepsilon \sigma_{xy}|_{E_F}$ (consistent with the low- T Mott relation) and ultimately to the relocation/intensity change of *strongly peaked* Berry-curvature hot spots associated with SOC-opened avoided crossings in Co-3d bands. Device-level figures of merit, including the ANE thermopower S_{ANE} and Ettingshausen coefficient $\Pi_{\text{AEE}} = T S_{\text{ANE}}$, show robust switching at a fixed temperature (e.g., 300 K) under a constant in-plane bias current, enabling compact, current-driven, sensor-free thermal control.

The materials-level thresholding demonstrated in DyCo_5 provides a practical design parameter for $R\text{Co}_5$ and related ferromagnets: Compositions, strain states, and anisotropy engineering that sharpen $\partial_\varepsilon \sigma_{xy}$ near E_F are expected to enhance α_{xy} and improve switching contrast, provided longitudinal losses remain modest.

- ¹E. Pop, *Nano Res.* **3**, 147–169 (2010).
- ²A. L. Moore and L. Shi, *Materials Today* **17**, 163–174 (2010).
- ³K.-i. Uchida, W. Zhou, and Y. Sakuraba, *Appl. Phys. Lett.* **18**, 140504 (2021).
- ⁴W. Nernst, *Annalen der Physik* **267**, 760–789 (1887).
- ⁵A. V. Ettingshausen and W. Nernst, *Annalen der Physik* **265**, 343–347 (1886).
- ⁶N. Nagaosa, J. Sinova, S. Onoda, A. H. MacDonald, and N. P. Ong, *Rev. Mod. Phys.* **82**, 1539–1592 (2010).
- ⁷A. Miura, H. Sepehri-Amin, K. Masuda, H. Tsuchiura, Y. Miura, R. Iguchi, Y. Sakuraba, J. Shiomi, K. Hono, and K. Uchida, *Appl. Phys. Lett.* **115**, 222403 (2019).
- ⁸T. Tsushima and M. Ohkoshi, *Journal of Magnetism and Magnetic Materials* **31-34**, 197 (1983).
- ⁹A. Vishina, K. Skokov, H. Tsuchiura, P. Thunström, A. Aubert, O. Gutflisch, O. Eriksson, and H. C. Herper, arXiv:2511.17087 (2025).
- ¹⁰M. Ohkoshi, H. Kobayashi, T. Katayama, M. Hirano, and T. Tsushima, *Physica B+C* **86**, 195 (1977).
- ¹¹I. S. Tereshina, N. L. Korenovskii, G. S. Burkhanov, M. D. Kuz'min, K. P. Skokov, and J. J. Meler, *Journal of Experimental and Theoretical Physics* **105**, 1230 (2007).
- ¹²K. P. Belov, A. K. Zvezdin, A. M. Kadomtseva, and R. Z. Levitin, *Sov. Phys. Usp.* **19**, 574 (1976).
- ¹³J. Dorantes-Dávila, R. Garibay-Alonso, and G. M. Pastor, *Phys. Rev. B* **110**, 174406 (2024).
- ¹⁴N. F. Mott and H. Jones, *Theory of the Properties of Metals and Alloys*. Oxford University Press, Reprinted by Dover Publications, New York. (1936).
- ¹⁵M. Cutler and N. F. Mott, *Phys. Rev.* **181**, 1336 (1969).
- ¹⁶T. Seki, R. Iguchi, K. Takanashi, and K. Uchida, *J. Phys. D: Appl. Phys.* **51**, 254001 (2018).
- ¹⁷P. Blaha, K. Schwarz, G. K. Madsen, D. Kvasnicka, J. Luitz, *et al.*, An augmented plane wave+ local orbitals program for calculating crystal properties **60** (2001).
- ¹⁸J. P. Perdew, K. Burke, and M. Ernzerhof, *Phys. Rev. Lett.* **77**, 3865 (1996).
- ¹⁹A. I. liechtenstein, V. I. Anisimov, and J. Zaanen, *Phys. Rev. B* **52**, R5467–R5470 (1995).
- ²⁰G. Pizzi, V. Vitale, R. Arita, S. Blügel, F. Freimuth, G. Géranton, M. Gibertini, D. Gresch, C. Johnson, T. Koretsune, *et al.*, *Journal of Physics: Condensed Matter* **32**, 165902 (2020).
- ²¹N. Marzari, A. A. Mostofi, J. R. Yates, I. Souza, and D. Vanderbilt, *Rev. Mod. Phys.* **84**, 1419 (2012).
- ²²G. K. H. Madsen, J. Carrete, and M. J. Verstraete, *Comput. Phys. Commun.* **231**, 140 – 145 (2018).
- ²³D. Xiao, Y. Yao, Z. Fang, and Q. Niu, *Phys. Rev. Lett.* **97**, 026603 (2006).

²⁴D. Xiao, M.-C. Chang, and Q. Niu, *Rev. Mod. Phys.* **82**, 1959–2007 (2010).

²⁵M. Ikhlas, T. Tomita, T. Koretsune, M.-T. Suzuki, D. Nishio-Hamane, R. Arita, Y. Otani, and S. Nakatsuji, *Nature Physics*

13, 1085–1090 (2017).

²⁶T. S. Seifert, U. Martens, F. Radu, M. Ribow, M. Berritta, L. Nádvořník, R. Starke, T. Jungwirth, M. Wolf, I. Radu, M. Münzenberg, P. M. Oppeneer, G. Woltersdorf, and T. Kampfrath, *Adv. Mater.* **33**, 2007398 (2021).